Journal of Crystal Growth 340 (2012) 190–196

Contents lists available at SciVerse ScienceDirect

Journal of Crystal Growth

journal homepage: www.elsevier.com/locate/jcrysgro

Role of characteristic modes in the dynamics of wave pattern in the Czochralski oxide crystal growth

C.J. Jing [a,c,*], C.X. Jia [b], K. Li [c], H. Arima [d]

[a] College of Architecture and Environment, Sichuan University, Chengdu 610064, China
[b] Sichuan College of Architectural Technology, Deyang 618000, Sichuan, China
[c] Key Laboratory of Microgravity, Institute of Mechanics, Chinese Academy of Sciences, Beijing 100190, China
[d] Institute of Ocean Energy, Saga University, Saga 840-8502, Japan

ARTICLE INFO

Article history:
Received 10 May 2011
Received in revised form
2 December 2011
Accepted 5 December 2011
Communicated by J.J. Derby
Available online 13 December 2011

Keywords:
A1. Characteristic mode
A1. Fluid flows
A1. Proper orthogonal decomposition
A1. Wave pattern
A2. Czochralski method
B1. Oxides

ABSTRACT

Wave pattern is a flow pattern observed on the free surface of oxide melt in the Czockralski crucible. Wave pattern exhibits regular folds in the azimuthal direction. In this paper three-dimensional flows of the $LiNbO_3$ melt in a Czockralski crucible of radius $r_c=100$ mm and crystal radius $r_s=50$ mm were investigated. The crucible is still and the crystal is rotating at a rate Ω_s. The flow is assumed to be laminar. The governing equations of the melt flows were solved by a block-structured boundary-fitted-coordinate method. Massive numerical simulations were first conducted to obtain several stable n-folded wave patterns by changing aspect ratio $A=h/r_c$ and Ω_s, where h is the depth of the oxide melt. The proper orthogonal decomposition was then applied to extract the characteristic modes of the n-folded original wave patterns. The spatial feature of the characteristic modes and the role of the characteristic modes in the dynamic process of the original wave patterns were finally analyzed. Some interesting conclusions are obtained. The characteristic modes of the wave patterns show strong spatial feature. The characteristic modes have more folds in the azimuthal direction than the original wave patterns; the characteristic modes appear in group; with the increase of group order, the number of folds in the azimuthal direction is increased regularly by n for the n-folded original wave pattern. The study of the dynamic process shows that the original wave pattern is a traveling wave, which is formed by the dominant characteristic modes.

1. Introduction

In the Czochralski crystal growth system the so-called wave patterns were observed in the 1980s [1–8]. The patterns appear on the free surface of oxide melt in the Czochralski crucible. Concerning the wave patterns, Jones made a lot of experimental studies [1–4], Seidl et al. [5], Enger et al. [6], Kumar et al. [7] and Jing et al. [8] reported some theoretical models and numerical simulations. These studies focused on the macroscopic flow patterns. Jones reproduced the wave patterns by a 'cold model' experiment and investigated the mechanism of the wave patterns. The general conclusions are that the wave patterns result from the baroclinic instability. Theoretical investigations such as the works of Enger et al. [6] and Jing et al. [8] mainly focused on the evolution and the three-dimensional spatial structures of the wave patterns by numerical simulations. There are few studies on the characteristic modes of the wave patterns. The characteristic modes are the modes, which construct the wave patterns. Between the original wave pattern and the characteristic modes must exist a tight connection. In order to better understand the wave patterns it is very helpful to reveal the features and the roles of the characteristic modes of the wave patterns. In addition, it is attractive to clarify the formation dynamics of the wave patterns from the characteristic modes. Therefore, it is necessary to investigate the roles of the characteristic modes in the wave patterns. In this paper, numerous massive simulations were first conducted to obtain some stable wave patterns, and then use of proper orthogonal decomposition was made to extract the characteristic modes of the obtained wave patterns. Finally the spatial features of the characteristic modes and the roles of the characteristic modes in the dynamics of wave patterns were investigated and summarized.

2. Numerical simulation of wave pattern

2.1. Physical model

The geometry of the problem to be studied is depicted in Fig. 1(a). The cylindrical crucible is static and the crystal is

* Corresponding author. Tel./fax: +86 28 85226855.
E-mail address: chengjunjing@126.com (C.J. Jing).

0022-0248/$ - see front matter © 2011 Elsevier B.V. All rights reserved.
doi:10.1016/j.jcrysgro.2011.12.033

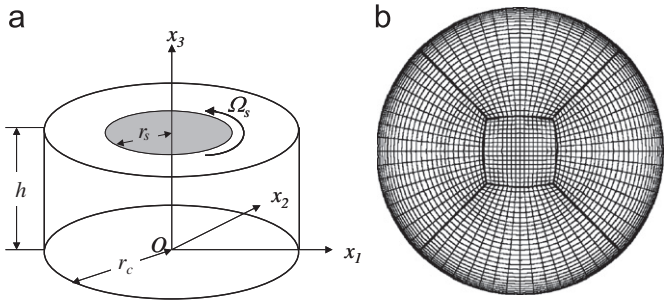

Fig. 1. Coordinate system (a) and block-structured grid (b).

Table 1
Transport variable Φ, dimensionless parameter R_Φ, source term S_Φ and S^*_Φ in mass, momentum and energy equations (see Eqs. (1) and (6)).

Variable	Φ	R_Φ	S_Φ	S^*_Φ
Mass	1	∞	0	0
Momentum(j-th comp.)	U_j	Re	$-\frac{\partial P}{\partial X_j}+F$	$-\frac{\partial \xi_k}{\partial X_j}\frac{\partial P}{\partial \xi_k}+F$
Energy	T	$PrRe$	0	0

where $F=\frac{Gr}{Re^2}\delta_{j3}(T-1)$.

rotating at Ω_s rpm. The radius and height of the crucible are r_c and h, respectively. The radius of the crystal is r_s. The free surface of the melt and the melt/crystal interface were treated as flat. The oxide melt was assumed to be an incompressible Newtonian Boussinesq fluid. The temperature of the melt/crystal interface was maintained at the melting point, T_m. The heat loss from the free surface of the melt was assumed to be due to radiation alone to an ambient temperature, $\overline{T}_a$. The sidewall of the crucible was heated by a constant and uniform heat flux, $\overline{q}_c$. The bottom of the crucible was adiabatic. The no-slip condition was used for all physical boundaries of the melt. The free surface was considered to be free of stresses.

2.2. Mathematical formulation and numerical method

The dimensionless governing equations for the melt flow in the Cartesian coordinates can be generally written as [8]

$$\left(\frac{\partial \Phi}{\partial \tau}+\frac{\partial U_i \Phi}{\partial X_i}\right)-\frac{1}{R_\Phi}\frac{\partial}{\partial X_i}\left(\frac{\partial \Phi}{\partial X_i}\right)=S_\Phi, \tag{1}$$

where Φ denotes a general transport variable, X_i the i-th Cartesian coordinate, U_i the i-th Cartesian velocity component, τ the time, S_Φ the source of Φ and R_Φ a dimensionless parameter. Table 1 gives the values of Φ, S_Φ and R_Φ for all transport equations used in the model. In contrast to what is reported by Basu et al. [9], the dissipative terms due to viscous effects were neglected in the energy equation. In Table 1, P is the pressure and T is the temperature of the melt. The definition of the dimensionless parameters are $Gr=g\beta T_m r_c^3/\nu^2$, $Pr=\nu/\alpha$ and $Re=u_{ref}r_c/\nu$, where g is the gravitational acceleration, β is the coefficient of volumetric thermal expansion, μ is the dynamic viscosity, ν is the kinematic viscosity, α is the thermal diffusivity and u_{ref} is the characteristic velocity.

The boundary conditions can be written as:

At the melt/crystal interface:

$$U_1=-\mathrm{Re}_s R\sin\theta/\mathrm{Re},\quad U_2=\mathrm{Re}_s R\cos\theta/\mathrm{Re},\quad U_3=0,\quad T=1 \tag{2}$$

where $R=\sqrt{X_1^2+X_2^2}$ and $\theta=\tan^{-1}(X_2/X_1)$.

At the free surface:

$$\partial U_i/\partial X_3=0,\quad i=1,\ 2,\quad U_3=0,\quad -\partial T/\partial X_3=R_{rad}(T^4-T_a^4) \tag{3}$$

At the sidewall of the crucible:

$$U_i=0,\ i=1,2,3,\quad \partial T/\partial \boldsymbol{n}=q_c \tag{4}$$

At the bottom of the crucible:

$$U_i=0,\ i=1,2,3,\quad \partial T/\partial X_3=0 \tag{5}$$

where $\boldsymbol{n}$ denotes the normal distance to the boundary. The dimensionless parameters are $\mathrm{Re}_s=r_c^2\omega_s/\nu$ and $R_{rad}=\varepsilon\sigma T_m^3 r_c/\lambda$, where $\omega_s=2\pi\Omega_s/60$ is the angular velocity of the crystal, ε is the emissivity, σ is the Stefan-Boltzmann constant and λ is the thermal conductivity.

In deriving the above equations, the characteristic length, velocity, temperature, pressure and time are, respectively,

$$l_{ref}=r_c,\quad u_{ref}=\nu/r_c,\quad T_{ref}=T_m,\quad P_{ref}=\rho u_{ref}^2,\quad t_{ref}=l_{ref}/u_{ref}$$

2.3. Block-structured grid

Owing to the several advantages discussed in [9], a block-structured grid [10–12] with matching/nonoverlapping interfaces was adopted in the present study. The domain was divided into five blocks and each block was further subdivided into finite control volumes. The top view of the block-structured grid is shown in Fig. 1(b), where the bold lines show the borders between the two blocks. The actually used grids are twice as fine as those shown in Fig. 1(b) and the number of the total control volumes is 476160. For the vertical direction, each block has the identical non-uniform grid assignment.

2.4. Governing equations in curvilinear coordinates

Because of the nonorthogonality of the grids and the curvilinear boundaries, the boundary-fitted-coordinate method (BFC) [13,14] was adopted. The governing equation, Eq. (1), in the physical space (X_i, $i=1,2,3$) was first transformed to the computational space (ξ_i, $i=1,2,3$) and takes the following form after the coordinate transformation [10,11].

$$\left(\frac{\partial \Phi}{\partial \tau}+\frac{1}{J}\frac{\partial U_k^* \Phi}{\partial \xi_k}\right)-\frac{1}{R_\Phi}\frac{1}{J}\frac{\partial}{\partial \xi_k}\left(Jg_{kl}\frac{\partial \Phi}{\partial \xi_l}\right)=S_\Phi^*, \tag{6}$$

Where

$$J=\frac{\partial(X_1,X_2,X_3)}{\partial(\xi_1,\xi_2,\xi_3)}\ \text{and}\ g_{kl}=\frac{\partial \xi_k}{\partial X_i}\frac{\partial \xi_l}{\partial X_i}$$

J is the Jacobian matrix and g_{kl} is the metric tensor.

In Eq.(6), U_k^* is the contravariant velocity, which is defined as

$$U_k^*=JU_j\partial\xi_k/\partial X_j. \tag{7}$$

S_Φ^* is the source term after the coordinate transformation and is given in Table 1.

2.5. Estimation of the metrics

Unlike the commonly used method, we applied the shape function used in the finite element method to estimate the derivatives related to the coordinate transformation $\partial X_i/\partial\xi_j$, of which X_i was expressed as $X_i=\sum_{n=1}^{8}\varphi_n(\xi_1,\xi_2,\xi_3)X_i^n$, $i=1,2,3$. $\varphi_n(\xi_1,\xi_2,\xi_3)$ is the shape function and subscript n denotes the corner points of the control volume. This method was found to be able to improve the accuracy of the Jacobian matrix and the metric tensor.

2.6. Discretization and numerical method

Eq. (6) was discretized using a fully conservative finite-volume method with a non-staggered arrangement of the variables [15,16]. Central difference was used for all spatial derivatives and first-order forward difference for the time derivatives. For the convective term, QUICK scheme [17] was applied. Based on the continuity equation, a pressure-correction equation is derived according to SIMPLE algorithm [18]. To ensure the correct coupling of pressure and velocity fields, the well-known momentum interpolation technique of Rhie and Chow [15] was applied. The time interval $\Delta\tau=1.123\times10^{-5}(\Delta t=0.01\text{s})$ was tested to be suitable. The thermophysical properties of the $LiNbO_3$ melt are listed in Ref. [8].

2.7. Simulation of wave patterns

In order to obtain calculation conditions under which a stable wave pattern occurs, we conducted numerous numerical calculations. Table 2 shows the calculation cases we conducted. In the table, A is the aspect ratio, which is defined as $A=h/r_c$ and n is the number of the folds of the wave patterns. It should be noted that n indicates the number of folds of all temporarily appeared wave patterns independently of the time that the wave patterns last. The so-called 'temporarily appeared' wave patterns mean that the patterns appear at least once during the flow development. For our purpose only the stable patterns are desirable and acceptable. The stable two-folded, three-folded and four-folded wave patterns obtained in our calculations are indicated by an underlined number in Table 2. Fig. 2 shows the representative two-folded, three-folded and four-folded wave patterns. What is shown in Fig. 2 is a snapshot of temperature distribution on the melt free surface. The wave patterns indeed rotate with the crystal but at a much lower rotation rate. During the rotation, the patterns may have a slight deformation but the number of the folds does not change.

Table 2
Number of folds n of the wave patterns at various sets of aspect ratio A and crystal rotation rate Ω_s (rpm). The underlined numbers indicate the cases of stable wave patterns; the other numbers correspond to temporarily appeared wave patterns.

Ω_s	12	14	15	16	18	20	25
A				n			
0.2	3	3, 4	2,3,4	–	–	–	2,4
0.5	**2**,3	2,4	2,**3**,4,5	–	2,4	4	–
0.8	–	–	–	4,5	2,3,4,5	4	4,5,6
1	–	2,3,4	2,3,4,6	2,3,4,6	2,3,4	2,3,4,5	**4**,5,6

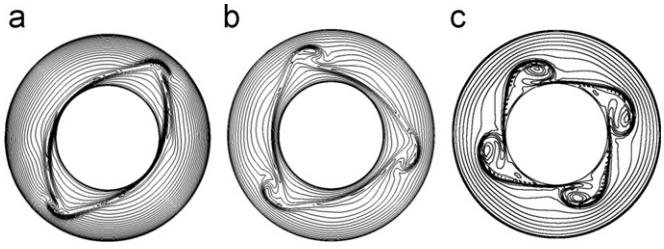

Fig. 2. Instantaneous temperature fields expressed through the contours of temperature for the typical two-folded wave pattern (a), three-folded wave pattern (b) and four-folded wave pattern (c). These patterns are obtained at (a) $A=0.5$, $\Omega_s=12$ rpm, (b) $A=0.5$, $\Omega_s=15$ rpm, (c) $A=1$, $\Omega_s=25$ rpm. The Grashof number and the Prandtl number are $Gr=2.02\times10^7$ and $Pr=13.6$, respectively, which correspond to the physical property of the $LiNbO_3$ melt.

3. The spatial characteristic modes of the wave patterns

3.1. The way of obtaining the characteristic modes

The way to obtain the characteristic modes of the wave patterns is proper orthogonal decomposition (POD). Since the initial work of Lumley [19], POD has been widely applied to analysis of flows. Especially after Sirovich [20,21] proposed a so-called method of snapshots, the use of POD to extract the characteristic modes of a complicated flow becomes feasible. The method of snapshots, which is applied to our problem is presented in a practical way in the following [22,23].

The state variable that we choose is the temperature field, $T(\boldsymbol{x},\tau)$. The temperature field is decomposed into time-averaged parts, $\overline{T}(\boldsymbol{x})$, and time-varying parts, $T'(\boldsymbol{x},\tau)$, i.e.,

$$T(\boldsymbol{x},\tau)=\overline{T}(\boldsymbol{x})+T'(\boldsymbol{x},\tau) \tag{8}$$

From the time-varying temperature field, we construct the two-time correlation matrix,$C_{m,n}$, as

$$C_{m,n}=\frac{1}{N}\int_D (T'(\boldsymbol{x},\tau_m)\times T'(\boldsymbol{x},\tau_n))d\boldsymbol{x},\quad m,n=1,2,\ldots,N \tag{9}$$

where N is the number of the snapshots of the temperature field and D is the flow domain.

By calculating the eigenvalues λ_i associated to the above matrix, and their corresponding eigenvectors A_i^m, $m=1,N$, which gives

$$C_{m,n}A_i^n=\lambda_i A_i^m, \tag{10}$$

we can obtain the characteristic modes $\Theta_i(\boldsymbol{x})$ (here normalized) as linear combinations of the time-varying parts,

$$\Theta_i(\boldsymbol{x})=\sum_{m=1}^{N} A_i'^m T'(\boldsymbol{x},\tau_m), \tag{11}$$

where $A_i'^m=A_i^m/\sqrt{\lambda_i N\sum_{m=1}^{N}(A_i^m)^2}$.

The time-varying parts $T'(\boldsymbol{x},\tau)$ can then be expressed in terms of the characteristic modes as

$$T'(\boldsymbol{x},\tau)=\sum_{i=1}^{M} a_i(\tau)\Theta_i(\boldsymbol{x}) \tag{12}$$

where $a_i(\tau)$ are coefficients depending on time, and $M$are the numbers of the first most important characteristic modes retained in the expansion. When $M=N$, the original temperature field can be reproduced exactly, with

$$a_i(\tau)=a_i^m=N\lambda_i A_i'^m. \tag{13}$$

Usually, M is much smaller than the number of snapshots, N. It is chosen so that the set of the characteristic modes captures most of the fluctuation energy. For example in Sirovich [20,21], the choice is made by taking $\xi>99\%$, where $\xi\equiv\sum_{i=1}^{M}\lambda_i/\sum_{i=1}^{N}\lambda_i$, meaning that the first M characteristic modes capture more than 99% of the fluctuation thermal energy.

3.2. The characteristic modes of the two-folded wave pattern

We first chose the two-folded wave pattern as shown in Fig. 2(a) to investigate the characteristic modes and their spatial feature. The sample covering several quasi-periods was chosen first. Then for the chosen sample, the number of snapshots, N, was determined by its effect on the eigenvalues of the two-time correlation matrix. The eigenvalues tend to be fixed with the increase of N. The number of snapshots, N, for the chosen sample, may be changed by changing the inter-snapshot interval. In this study it was found that $N=100$ is enough (the variance of the most important eigenvalues is less than about 5%). The time evolution of the temperature during the sample duration at a

monitoring point on the melt free surface ($R=0.75$, $\theta=0$) is shown in Fig. 3.

Fig. 4 shows the first six characteristic modes, $\Theta_i(x)$, for the two-folded original wave pattern ($n=2$, Fig. 2(a)). In each case, the contours of the perturbation temperature field, $T'(\boldsymbol{x},\tau)$, at the free surface are plotted. Positive (negative) perturbations are plotted as solid (dotted) lines. We see that the characteristic modes exhibit clear spatial features. If we define an elementary pattern as an area in which the temperature perturbation has neighboring positive and negative contributions, we see that: (1) the characteristic modes may contain more elementary patterns than the number of folds in the original wave pattern, (2) the characteristic modes appear in groups (Fig. 4(a) and (b) show the first group, Fig. 4(c) and (d) the second group and, Fig. 4(e) and (f) the third group), and pair of two similar characteristic modes appears as i-th group, and (3) the wave number of the i-th group's characteristic modes (l_i) is given as $l_i=n\times i$ (in the case $n=2$). On the other hand, in the radial direction the number of the elementary patterns is also increased with the group order but the regularity is not as clear as in the azimuthal direction.

The characteristic modes give different contributions to the original pattern. From Table 3 it can be seen again clearly that the characteristic modes appear in group. The first group (characteristic modes 1 and 2) contributes about 22% and 21%, the second group (characteristic modes 3 and 4) contributes about 8.0% and 7.8%, the third group (characteristic modes 5 and 6) contributes about 3.1% and 2.8% to the total fluctuation energy, respectively. With the increase of the group order, the contribution is decreased, and the first ten characteristic modes capture almost 72% of the total energy. 99% of the feature of the two-folded wave pattern shown in Fig. 2(a) may be captured by the first 80 characteristic modes.

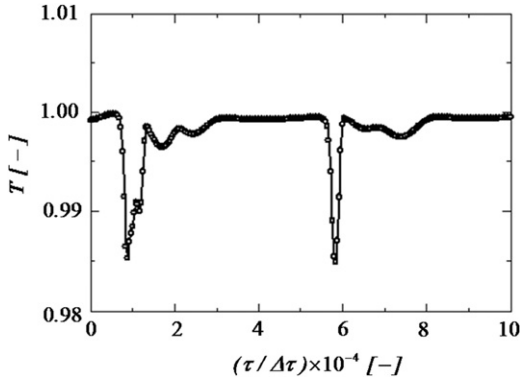

Fig. 3. Time evolution of the dimensionless temperature T at a monitoring point on the melt free surface ($R=0.75$, $\theta=0$) for the two-folded wave pattern as shown in Fig. 2(a).

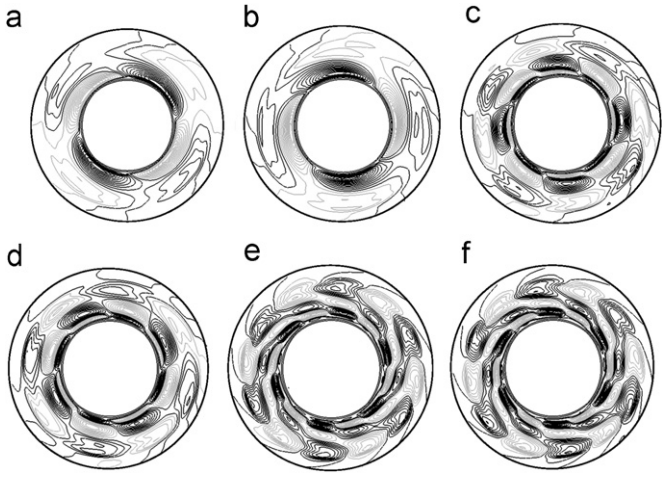

Fig. 4. Contours of temperature for the first six characteristic modes of the two-folded wave pattern. The characteristic modes are obtained by POD from a sample composed of $N=100$ snapshots of temperature field.

Table 3
Eigenvalues of the most energetic modes and their cumulative contribution to the original two-folded wave pattern at $A=0.5$ and $\Omega_s=12$ rpm. The Grashof number and the Prandtl number are $Gr=2.02\times10^7$ and $Pr=13.6$, respectively.

Index of the mode	Eigenvalue λ_i	Cumulative energy contribution (%)
1	0.3630×10^{-6}	22.436
2	0.3382×10^{-6}	43.343
3	0.1303×10^{-6}	51.398
4	0.1271×10^{-6}	59.253
5	0.5059×10^{-7}	62.380
6	0.4658×10^{-7}	65.259
7	0.3541×10^{-7}	67.448
8	0.3456×10^{-7}	68.584
9	0.2528×10^{-7}	71.146
10	0.1995×10^{-7}	72.380
20	0.1105×10^{-7}	80.484
50	0.4596×10^{-8}	92.898
80	0.2214×10^{-8}	99.064
100	0.1304×10^{-8}	100.00

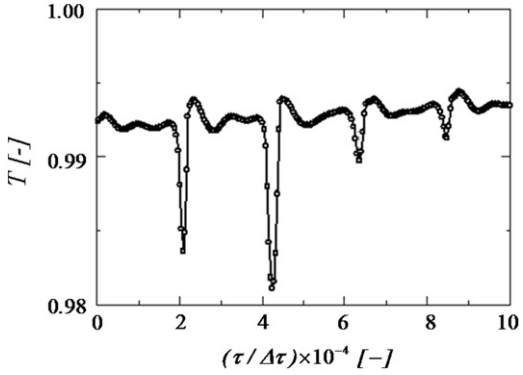

Fig. 5. Time evolution of the dimensionless temperature T at a monitoring point on the melt free surface ($R=0.75$, $\theta=0$) for the three-folded wave pattern as shown in Fig. 2(b).

3.3. The characteristic modes of the three-folded wave pattern

The number of snapshots chosen to extract the characteristic modes for the three-folded wave pattern is also $N=100$ and the time evolution of the temperature during the sample duration at the monitoring point is shown in Fig. 5. We see that the sample covers more than one rotation period of the three-folded wave pattern.

Fig. 6 shows the first nine characteristic modes, $\Theta_i(\boldsymbol{x})$, for the three-folded original wave pattern ($n=3$, Fig. 2(b)). We see that the characteristic modes also have a clear spatial feature. The feature is same as that for the two-folded wave pattern. But in this case the first group contains three characteristic modes. For the other groups, each group contains two characteristic modes (in pair). The wave number of the i-th group's characteristic modes (l_i) is given still as $l_i=n\times i$ (in the case $n=3$). In the radial direction, the number of the elementary patterns is increased with the group order but the regularity is not clear.

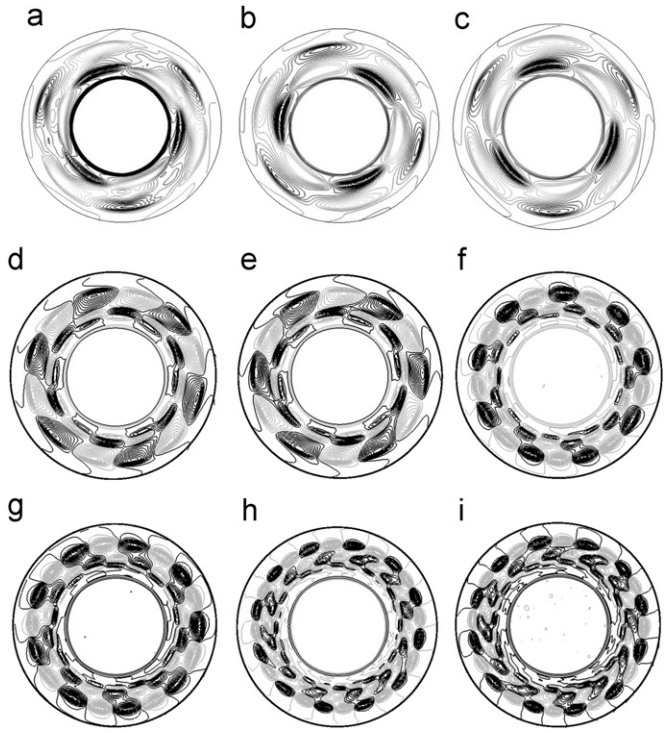

Fig. 6. Contours of temperature for the first nine characteristic modes of the three-folded wave pattern. The characteristic modes are obtained by POD from a sample composed of $N=100$ snapshots of temperature field.

Table 4
Eigenvalues of the most energetic modes and their cumulative contribution to the original three-folded wave pattern at $A=0.5$ and $\Omega_s=15$ rpm. The Grashof number and the Prandtl number are $Gr=2.02\times10^7$ and $Pr=13.6$, respectively.

Index of the mode	Eigenvalue λ_i	Cumulative energy contribution (%).
1	0.5028×10^{-6}	29.237
2	0.3157×10^{-6}	47.595
3	0.3067×10^{-6}	65.429
4	0.1032×10^{-6}	71.430
5	0.9686×10^{-7}	77.062
6	0.4551×10^{-7}	79.708
7	0.4486×10^{-7}	82.316
8	0.2422×10^{-7}	83.725
9	0.2403×10^{-7}	85.122
10	0.1501×10^{-7}	85.995
20	0.6075×10^{-8}	91.040
50	0.2155×10^{-8}	97.186
80	0.7248×10^{-9}	99.520
100	0.2054×10^{-9}	100.00

From Table 4 it can be seen again that the characteristic modes appear in group. The first characteristic mode contribute to about 29%, and the second and third characteristic mode (first group) contribute to about 18%, the characteristic modes 4 and 5 (second group) contribute to about 6%, the characteristic modes 6 and 7 (third group) contribute to about 2.6%, and the characteristic modes 8 and 9 (fourth group) contribute to about 1.4%. With the increase of the group order, the contribution decreases and the differences between the groups decrease as well. The first nine characteristic modes capture about 85% of the total energy, or, 85% of the feature of the three-folded wave pattern shown in Fig. 2(b) may be captured by the first nine characteristic modes. If 99.5% of the feature of the three-folded wave pattern shown in Fig. 2(a) is wanted to be captured, 80 characteristic modes are needed.

3.4. The characteristic modes of the four-folded wave pattern

Fig. 7 shows the time evolution of the temperature at the monitoring point for the four-folded wave pattern. Only the time period over which a sample of $N=100$ snapshots has been extracted is shown. Fig. 8 shows the first six characteristic modes for the four-folded original wave pattern ($n=4$, Fig. 2(c)). It can be seen that in this case the characteristic modes appear basically by groups of two, for example, Fig. 8(a) and (b) show the first group, Fig. 8(c) and (d) show the second group, Fig. 8(e) and (f) show the third group. The characteristic modes 1 and 2 have four elementary patterns in the azimuthal direction. A similar azimuthal dependence is found for the characteristic modes 3 and 4, but they have two elementary patterns in the radial direction. Finally, the characteristic modes 5 and 6 have eight elementary patterns in the azimuthal direction and two in the radial direction.

From Table 5 it can be seen again that the characteristic modes could be grouped. The first two characteristic modes (first group) contribute to about 28%, the characteristic modes 3 and 4 (second

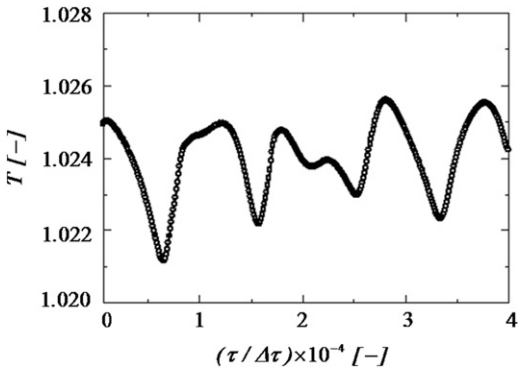

Fig. 7. Time evolution of the dimensionless temperature T at a monitoring point on the melt free surface ($R=0.75$, $\theta=0$) for the four-folded wave pattern as shown in Fig. 2(c).

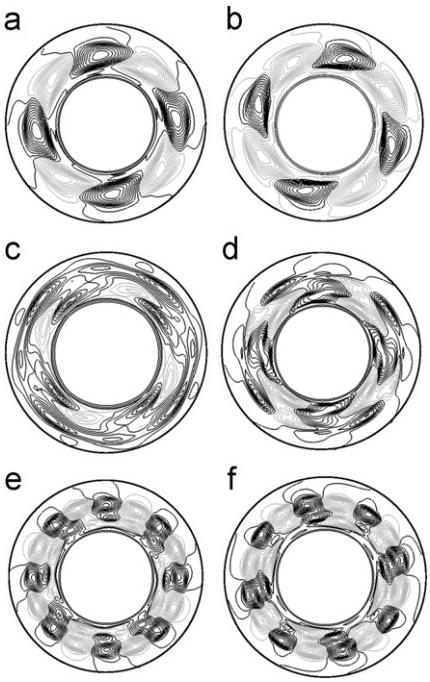

Fig. 8. Contours of temperature for the first six characteristic modes of the four-folded wave pattern. The characteristic modes are obtained by POD from a sample composed of $N=100$ snapshots of temperature field.

Table 5
Eigenvalues of the most energetic modes and their cumulative contribution to the original four-folded wave pattern at $A=1$ and $\Omega_s=25$ rpm. The Grashof number and the Prandtl number are $Gr=2.02\times10^7$ and $Pr=13.6$, respectively.

Index of the mode	Eigenvalue λ_i	Cumulative energy contribution (%)
1	0.1141×10^{-5}	28.881
2	0.1120×10^{-5}	57.233
3	0.3192×10^{-6}	65.310
4	0.3036×10^{-6}	72.992
5	0.2179×10^{-6}	78.508
6	0.2060×10^{-6}	83.722
7	0.1465×10^{-6}	87.431
8	0.1131×10^{-6}	90.293
9	0.9514×10^{-7}	92.700
10	0.6181×10^{-7}	94.264
20	0.5786×10^{-8}	99.627
30	0.1476×10^{-9}	99.993
50	0.2619×10^{-13}	100.00
100	0.1846×10^{-22}	100.00

group) contribute to about 8.0% and 7.6%, the characteristic modes 5 and 6 (third group) contribute to about 5.5% and 5.2%, respectively. The first six characteristic modes capture about 83% of the total energy.

4. The dynamic process of wave pattern

The dynamic process mentioned here is not a transition or an evolution process in the conventional meaning but the built-up of the wave pattern by the characteristic modes of the perturbation. First, let us see the mathematical formulation of wave pattern reconstruction. According to proper orthogonal decomposition, the temperature field at any time can be obtained by a linear combination of the characteristic modes as follows.

$$T(\boldsymbol{x},\tau)=\overline{T}(\boldsymbol{x})+T'(\boldsymbol{x},\tau)=\overline{T}(\boldsymbol{x})+\sum_{i=1}^{M}a_i(\tau)\Phi_i(\boldsymbol{x}) \tag{14}$$

where $\overline{T}(\boldsymbol{x})$ is the mean temperature, which is obtained by $\overline{T}(\boldsymbol{x})=(1/N)\sum_{i=1}^{N}T(\boldsymbol{x},\tau_i)$, and is only a function of space. M is the number of the characteristic modes used to reconstruct the overall temperature field. $\Phi_i(\boldsymbol{x})$, the i-th characteristic mode, is only a function of space. For the case of the two-folded wave pattern, $\Phi_i(\boldsymbol{x})$, $i=1,6$, are shown in Fig. 4. $a_i(\tau)$ denotes an instantaneous contribution of the i-th characteristic mode to the overall temperature field and is only a function of time. For the case of the two-folded wave pattern, $a_i(\tau)$, $i=1,3$, is shown in Fig. 9. We see that the characteristic modes Φ_1 and Φ_2 evolve in time with the same frequency whereas Φ_3 has a larger frequency, which is twice that of Φ_1 or Φ_2 and has a smaller contribution. The phase shift between a_1 and a_2 is $\pi/2$, however, it should be noted that two periods of a_1 and a_2 can roughly represent a 2π-rotation of the original two-folded pattern.

Fig. 10 shows the mean temperature field and the patterns of the temperature fields obtained by reconstruction with an increasing number of characteristic modes at $\tau=2.5\times10^4\Delta\tau$ ($t=250$s) inside the period shown in Fig. 9. It can be seen that with the increase of the number of the characteristic modes used to reconstruct the original pattern, i.e., with the increase of M in Eq. (14), the reconstructed pattern gets closer to the original pattern (Fig. 2(a)). From Table 3, we know that the first six characteristic modes capture about 65% of the total information of the two-folded pattern; therefore, the original two-folded pattern cannot be exactly reconstructed with only these six characteristic modes. On the other hand, for $M=100$, the reconstruction is exact.

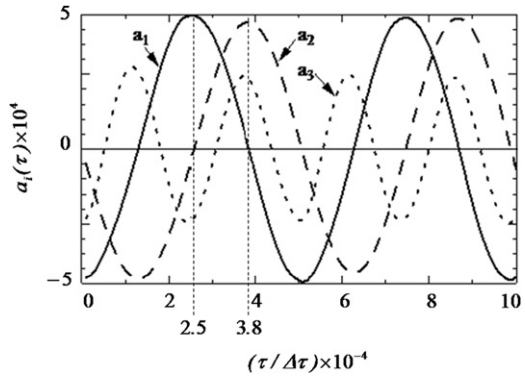

Fig. 9. Time variation of the coefficients $a_i(\tau)$, $i=1,3$, for the case of the two-folded wave pattern.

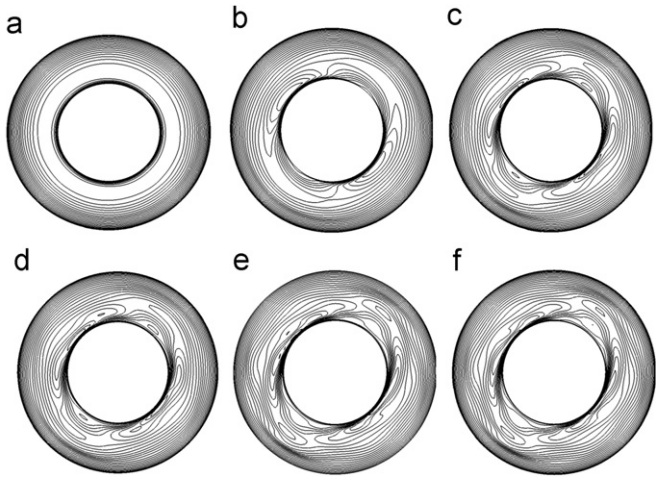

Fig. 10. Contours of the mean temperature field, (a), and the reconstructed temperature fields, (b)–(f), by POD using Eq. (14) with an increasing number, M, of characteristic modes at $\tau=2.5\times10^4\Delta\tau$($t=250$ s) inside the period shown in Fig. 10. (b) corresponds to $M=1$ (and also $M=2$, as $a_2=0$ at $\tau=2.5\times10^4\Delta\tau$ ($t=250$ s)), (c)–(f) correspond to $M=3,4,5,6$.

In the following, let us see the relationships between the original pattern and the characteristic modes. The two-folded wave pattern is taken as an example again. Fig. 11(a) and (b) show the original wave patterns at the instants $\tau_1=2.5\times10^4\Delta\tau$ ($t=250$s) and $\tau_2=3.8\times10^4\Delta\tau$($t=380$ s), respectively (see Fig. 9). As expected, we observe a rotation of the two-folded pattern in the azimuthal direction. On the other hand, Fig. 11(a) and (b) can be obtained exactly according to Eq. (14) with $M=100$. According to Eq. (14), the temperature field of the original wave pattern is formed by the mean temperature $\overline{T}(\mathbf{x})$ (Fig. 10(a)) and the temperature perturbations given by the characteristic modes (Fig. 4). We will first focus on the two first characteristic modes Φ_1 and Φ_2. Looking to Fig. 4(a) and (b), we see that Φ_2 has a similar structure as Φ_1, but this structure appears to have rotated by a quarter of an elementary pattern, i.e. by $\pi/4$. From Fig. 9, we know that at $\tau_1=2.5\times10^4\Delta\tau$ ($t=250$ s), the main perturbation is given by the first mode Φ_1 (the contribution of Φ_2 is zero). At $\tau_2=3.8\times10^4\Delta\tau=\tau_1+\Gamma/4$ ($\Gamma\approx5\times10^4\Delta\tau$ is the period for a π-rotation of the folds), the main perturbation is given by Φ_2 (the contribution of Φ_1 is zero). So the perturbation appears to have rotated by $\pi/4$. It is what we see in Fig. 11(a) and (b). At $\tau_3=\tau_1+\Gamma/2\approx5\times10^4\Delta\tau$, we have the main structure given by $-\Phi_1$ (the contribution of Φ_2 is zero). The elementary patterns are now those of Φ_1 but with changed signs, so that the perturbation appears to have rotated by $\pi/2$. At $\tau_4=\tau_1+3\Gamma/4\approx6.3\times10^4\Delta\tau$, the main perturbation structure is

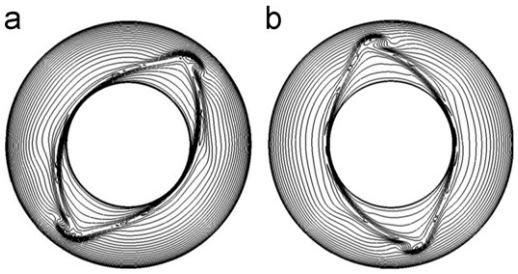

Fig. 11. Contours of temperature fields corresponding to $\tau=2.5\times10^4\Delta\tau$ ($t=250$ s) (a) and $\tau=3.8\times10^4\Delta\tau$ ($t=380$ s) (b) in Fig. 10 for the two-folded wave pattern. The spatial shift between (a) and (b) is about $\pi/4$.

given by $-\Phi_2$ (the contribution of Φ_1 is zero). The elementary patterns are now those of Φ_2 but with changed signs, so that the perturbation appears to have rotated by $3\pi/4$. We then see that for the two first characteristic modes, the observed combination of a spatial shift (rotation of $\pi/4$) and a temporal shift (time signals shifted by $\Gamma/4$) between them induces a traveling wave behavior. This analysis suggests that the rotation of the wave pattern is caused by the traveling wave behavior induced by the different pairs of characteristic modes.

5. Conclusion

Massive three-dimensional numerical simulations of the $LiNbO_3$ melt flow in a Czochralski crucible of radius $r_c=100$ mm and crystal radius $r_s=50$ mm were conducted. Some stable two-, three- and four-folded wave patterns were obtained numerically. For each stable wave pattern, proper orthogonal decomposition is applied to extract the characteristic modes. In this study the characteristic modes are shown by the perturbation temperature fields of the original wave patterns. By the analyses of the characteristic modes it is found that the characteristic modes of the wave patterns show some general spatial features: the characteristic modes appear in groups (pairs of modes); the characteristic modes may contain more elementary patterns than the folds of the original wave pattern; the number of the elementary patterns is generally increased by n with the increase of the group order for the n-folded wave pattern. In addition, the analyses of the dynamic process of the wave pattern indicate that the rotation of the original wave pattern in the azimuthal direction can be attributed to the traveling wave behavior of the characteristic mode pairs. These studies lead to a better understanding of the wave pattern appearing in the Czochralski oxide crystal growth.

Acknowledgment

Project 50876092 supported by NSFC. At the same time, this study was performed under the Cooperative Research Program of IOES, Institute of Ocean Energy, Saga University. (Accept#08005B).

References

[1] A.D.W. Jones, An experimental model of the flow in Czochralski growth, Journal of Crystal Growth 61 (1983) 235.
[2] A.D.W. Jones, Hydrodynamics of Czochralski growth—a review of the effects of rotation and buoyancy force, Progr. Crystal Growth Characterization 9 (1984) 139.
[3] A.D.W. Jones, The temperature field of a model Czochralski melt, Journal of Crystal Growth 69 (1984) 165.
[4] A.D.W. Jones, Flow in a model Czochralski oxide melt, Journal of Crystal Growth 94 (1989) 421.
[5] A. Seidl, G. McCord, G. Muller, H.J. Leister, Experimental observation and numerical simulation of wave patterns in a Czochralski silicon melt, Journal of Crystal Growth 137 (1994) 326.
[6] S. Enger, B. Basu, M. Breuer, F. Durst, Numerical study of three-dimensional mixed convection due to buoyancy and centrifugal force in an oxide melt for Czochralski growth, Journal of Crystal Growth 219 (2000) 144.
[7] V. Kumar, B. Basu, S. Enger, G. Brenner, F. Durst, Role of Marangoni convection in Si-Czochralski melts, part I: 3D predictions without crystal, Journal of Crystal Growth 253 (2003) 142.
[8] C.J. Jing, T. Tsukada, M. Hozawa, K. Shimamura, N. Ichinose, T. Shishido, Numerical studies of wave pattern in an oxide melt in the Czochralski crystal growth, Journal of Crystal Growth 265 (2004) 505.
[9] B. Basu, S. Enger, M. Breuer, F. Durst, Three-dimensional simulation of flow and thermal field in a Czochralski melt using a block-structured finite-volume method, Journal of Crystal Growth 219 (2000) 123.
[10] K.J. Badcock, B.E. Richards, M.A. Woodgate, Elements of computational fluid dynamics on block structured grids using implicit solvers, Progr, Progress in Aerospace Sciences 36 (2000) 351.
[11] F. Durst, M. Schafer, A parallel block-structured multigrid method for the prediction of incompressible flows, Journal for Numerical Method in Fluids 22 (1996) 549.
[12] W.L. Chen, F.S. Lien, M.A. Leschziner, Local mesh refinement within a multi-block structured-grid scheme for general flows, Computer Methods in Applied Mechanics and Engineering 144 (1997) 327.
[13] S. Sankaranarayanan, M.L. Spaulding, A study of the effects of grid non-orthogonality on the solution of shallow water equations in boundary-fitted coordinate systems, Journal of Computational Physics 184 (2003) 299.
[14] J.R. Pacheco, R.E. Peck, Non-staggered boundary-fitted coordinate method for free surface flows, Numerical Heat Transfer part B-Fundamentals 37 (2000) 267.
[15] C.M. Rhie, W.L. Chow, Numerical study of the turbulent flow past an airfoil with trailing edge separation, Journal of American Institute of Aeronautics and Astronautics 21 (1983) 1525.
[16] M.C. Liang, C.W. Lan, A finite-volume/Newton method for a two-phase heat flow problem using primitive variables and collocated grids, Journal of Computational Physics 127 (1996) 330.
[17] B.P. Leonard, The QUICK algorithm—A uniformly third-order finite-difference method for highly convective flows, Computer methods in fluids (A81-28303 11-34), Pentech Press, Ltd, London, 1980, pp. 159–195.
[18] S.V. Patankar, Numerical Heat Transfer and Fluid Flow, Hemisphere Publishing Corporation, 1980.
[19] J.L. Lumley, Toward a turbulent constitutive relation, Journal of Fluid Mechanics 41 (1970) 413.
[20] L. Sirovich, Turbulence and the dynamics of coherent structures. Part I: Coherent structures, Quarterly of Applied Mathematics 45 (1987) 561.
[21] L. Sirovich, H. Park, Turbulent thermal convection in a finite domain: Part I. Theory, Part II Numer. Results, Physics of Fluids A2 (1990) 1649.
[22] C.J. Jing, X.L. Liu, D. Henry, H. Ben Hadid, An application of proper orthogonal composition to the stability analysis of Czochralski melt flows, Journal of Crystal Growth 306 (2007) 166.
[23] K. Li, N. Imaishi, C.J. Jing, S. Yoda, Proper orthogonal decomposition of oscillatory Marangoni flow in half-zone liquid bridges of low-Pr fluids, Journal of Crystal Growth 307 (2007) 155.